Modeling phase transitions during the crystallization of a multicomponent fat under shear

Gianfranco Mazzanti,[1,2] Alejandro G. Marangoni,[2,1] and Stefan H. J. Idziak[1,*]

[1]*Department of Physics, and Guelph-Waterloo Physics Institute, University of Waterloo, Waterloo, Ontario, N2L 3G1 Canada*
[2]*Department of Food Science, University of Guelph, Guelph, Ontario, N1G 2W1 Canada*

The crystallization of multicomponent systems involves several competing physicochemical processes that depend on composition, temperature profiles, and shear rates applied. Research on these mechanisms is necessary in order to understand how natural materials form crystalline structures. Palm oil was crystallized in a Couette cell at 17 and 22 °C under shear rates ranging from 0 to 2880 s^{-1} at a synchrotron beamline. Two-dimensional x-ray diffraction patterns were captured at short time intervals during the crystallization process. Radial analysis of these patterns showed shear-induced acceleration of the phase transition from α to β'. This effect can be explained by a simple model where the α phase nucleates from the melt, a process which occurs independently of shear rate. The α phase grows according to an Avrami growth model. The β' phase nucleates on the α crystallites, with the amount of β' crystal formation dependent on the rate of transformation of α to β' as well as the growth rate of the β' phase from the melt. The shear induced α-β' phase transition acceleration occurs because under shear, the α nuclei form many distinct small crystallites which can easily transform to the β' form, while at lower shear rates, the α nuclei tend to aggregate, thus retarding the nucleation of the β' crystals. The displacement of the diffraction peak positions revealed that increased shear rate promotes the crystallization of the higher melting fraction, affecting the composition of the crystallites. Crystalline orientation was observed only at shear rates above 180 s^{-1} at 17 °C and 720 s^{-1} at 22 °C.

I. INTRODUCTION

The crystallization of multicomponent systems involves several competing physicochemical processes that depend on composition, temperature profiles, and shear rates applied. Research on these mechanisms is necessary in order to understand how natural materials form crystalline structures. To date, the knowledge of the effect that shear rates have on fat crystal structures formed under shear is still very limited [1–5]. The present study illustrates the effects of applied shear on the crystallization of palm oil, as part of a broader study on the behavior of fats crystallizing under shear [1–3]. Edible fats and oils are rather ubiquitous multicomponent materials of importance to both the food industry and retail consumers, and palm oil is the most important source of edible oils and fat in the world. A large proportion of palm oil is crystallized to fractionate the valuable fractions that occur naturally mixed in it, mostly olein (liquid fraction) and stearin (solid fraction). The success of a particular fractionation process, in terms of final crystal composition, structure, and morphology, is the result of the application of appropriate temperature and shear conditions to the melt.

Fats are composed mostly of triacylglycerols (TAG's)—i.e., a glycerol backbone esterified to three long-chain organic acids (fatty acids)—and a smaller fraction of polar lipids, mostly mono- and diacylglycerols.

The main fatty acids in palm oil triacylglycerols are myristic (abbreviated M, with 14 carbons and no double bonds, C14:0), palmitic (P, C16:0), stearic (S, C18:0), oleic (O, C18:1), and linoleic (L, C18:2). The palm oil from Malaysia (used in this study) contains about 94% TAG's and 4%–7.5% diacylglycerols. The four main TAG's are POP and POO forming ca. 55%, followed by POL with 9% and PPP with 6%, although of course there is some variability depending on the origin and extraction conditions [6–9].

Like many other fats, palm oil can crystallize in different phases, characterized by a particular composition and molecular arrangement or polymorphic form. The TAG molecules form lamellar structures by stacking in the longitudinal direction, usually of two (2L) or three (3L) fatty acid lengths. In our study we only observed crystals with 2L packing, as shown in Fig. 1(a). Typically, the crystals form platelike structures with molecules lying perpendicular to the flat surface. The more common polymorphic forms, analogous to those formed by pure triacylglycerols, are usually termed α, β', and β in order of increasing melting point, packing density, and thermodynamic stability. This polymor-
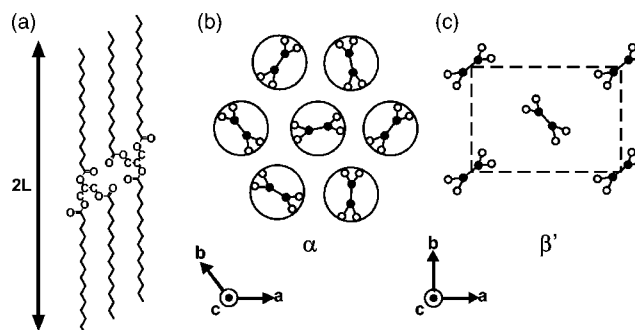

FIG. 1. (a) Sketch of the triacylglycerol molecules showing the 2L conformation found in the palm oil crystals. (b) Schematic of the in-plane packing of the TAG molecules in the α phase and (c) in the β' phase.

*Corresponding author. Electronic address: Idziak@uwaterloo.ca

TABLE I. Composition in terms of melting fractions of palm oil and its main derivatives [7].

	HMF	MMF	LMF
Palm oil, refined, bleached, and deodorized	11.1	45.9	43.0
Olein	2.8	47.6	49.6
Stearin	40.3	36.6	23.1

phism is a consequence of the variety of arrangements of lateral packing of the CH_2 groups of the triacylglycerol molecules in a fat crystal. In our study only α and β' forms were observed. The metastable α form, analogous to the rotator phase in alkanes [10], is associated with a hexagonal unit cell as shown in Fig. 1(b), the β' with an orthorhombic unit cell [4,11] as described schematically in Fig. 1(c). Thus knowledge of the lateral packing (e.g., α, β') and the longitudinal stacking (e.g., 2L) is required to describe the crystalline structure. In this study only 2L forms were observed; thus, we will call the phases simply α and β'. These structures can be characterized and differentiated by their characteristic x-ray diffraction patterns. The smaller repeating spacings of the lateral packing produce wide-angle x-ray reflections, while the longitudinal long spacings produce x-ray reflections in the small-angle region.

Upon cooling from the melt to temperatures below 24 °C, the first crystals to be observed appear in the metastable α phase and have a high concentration of MMM, PPP, PPS, POS, and POP. After that, palm oil undergoes a phase transition to form β' crystallites that are particularly stable over time, rather than forming β crystallites, while incorporating more of the lower melting component rich in POO, PLP, and SOO. The liquid phase is mostly PLO, OOO, PLL, and LOO [8,12–14]. Hence, the fractionation process is not simply a clear "cut" between two single different components, but rather a process of distribution of TAG's and diacylglycerols between the liquid phase and one or more solid phases.

The distribution of the diacylglycerols between olein and stearin also shows a fractionation process, since PO and OO have more affinity for the olein fraction, while more PP tends to crystallize with the stearin [15].

The families of TAG's are often grouped according to their crystallization and melting temperatures; hence, these groups are called melting fractions. The high melting fraction (HMF) contains saturated TAG's, rich in palmitic and myristic acid, and diacylglycerol PP. The medium melting fraction (MMF) contains mono-unsaturated TAG's (with one oleic or linoleic acid), while the low melting fraction (LMF) contains the balance of TAG's, including the diacylglycerols OO and PO [8]. It must be noted that actual phases will have somewhat different composition depending on crystallization conditions. These fractions do not crystallize in a completely independent fashion, since crystallization conditions affect the overall TAG distribution in the solid state. A typical composition of palm oil (refined, bleached and deodorized) and its main commercial fractions is presented in Table I.

Commercial dry fractionation often separates only 60% of the palm oil as olein [16]. With the use of pressure membrane filters, better separation is possible, in the range 20%

of stearin and 80% olein [17]. At 22 °C the proportion of solid fat content (SFC) accounted for by the high melting fraction is higher than at 17 °C, where more of the medium melting fraction is incorporated into the solid phase [18,19].

An additional piece of information from the literature is that the stable β' crystallites are known to form spherulitic clusters or polycrystals, from 10 μm up to 60 μm in size [12,20]. These spherulites can in turn agglomerate to form larger flocs of up to 600 μm in size [20]. This fact will serve to explain some of the crystallization behavior observed in our experiments.

In this paper we present a quantitative model describing the growth of crystals and shear-related phase transitions in palm oil.

II. METHODS

The melted sample was placed in the 1-mm gap of a Couette shear cell as illustrated in Fig. 2(a) [2]. The sample was kept at 50 °C and sheared at the selected shear rate for 30 min. Then the system was cooled at 3 °C/min to either 17 or 22 °C, while maintaining the shear in the cell. The system was then sheared at this final temperature until the experiment was ended, typically after 60 min. The shear rates used ranged from 45 to 2880 s^{-1}, where the average shear rate $\dot{\gamma}$ can be approximated by the relative velocity of the two shearing cylinders divided by the gap separating them ($\dot{\gamma} = \nu/\delta$). As a control, the sample was also cooled in the cell without applied shear—i.e., 0 s^{-1}.

The experiments were conducted at the ExxonMobil beamline X10A at the National Synchrotron Light Source in Brookhaven National Laboratory, Upton, NY, USA. A Bruker 1500 two-dimensional (2D) charge-coupled-device (CCD) detector was used to capture diffraction patterns with exposure times of 20 s or 50 s. The x rays had a wavelength $\lambda = 1.097$ Å and the detector was located 1132 mm from the cell axis for the small-angle x-ray diffraction experiments. The beam size of 0.5×0.5 mm^2 gave an instrumental resolution of 0.0023 Å^{-1}. The preliminary wide-angle x-ray diffraction experiments were performed with the detector located 150 mm from the cell.

The x-ray diffraction intensity from each 2D diffraction image, as illustrated in Fig. 2(b), was radially averaged and plotted as a function of the reciprocal lattice spacing q, where $q = 2\pi/d = 4\pi \sin(\theta)/\lambda$, d is the interplanar spacing, and 2θ is the Bragg angle as seen in Fig. 2(c). This radial averaging is accomplished by circular integration of the observed x-ray intensity at a fixed value of the radius r and repeating for all radial distances. The scattering angle corresponding to a given radial position can be calculated as $2\theta = \tan^{-1}(r/L)$ where L is the distance separating the flowing sample and the detector.

These radial averages of the resulting diffraction patterns were obtained using a custom plug-in program developed by us for the IMAGEJ software [21], which also allows for proper normalization of the intensities with respect to the incident beam and the correction of the intensity distortion introduced by the asymmetrical absorption from the cylindrical shape of the Couette cell. The resulting one-dimensional powder dif-
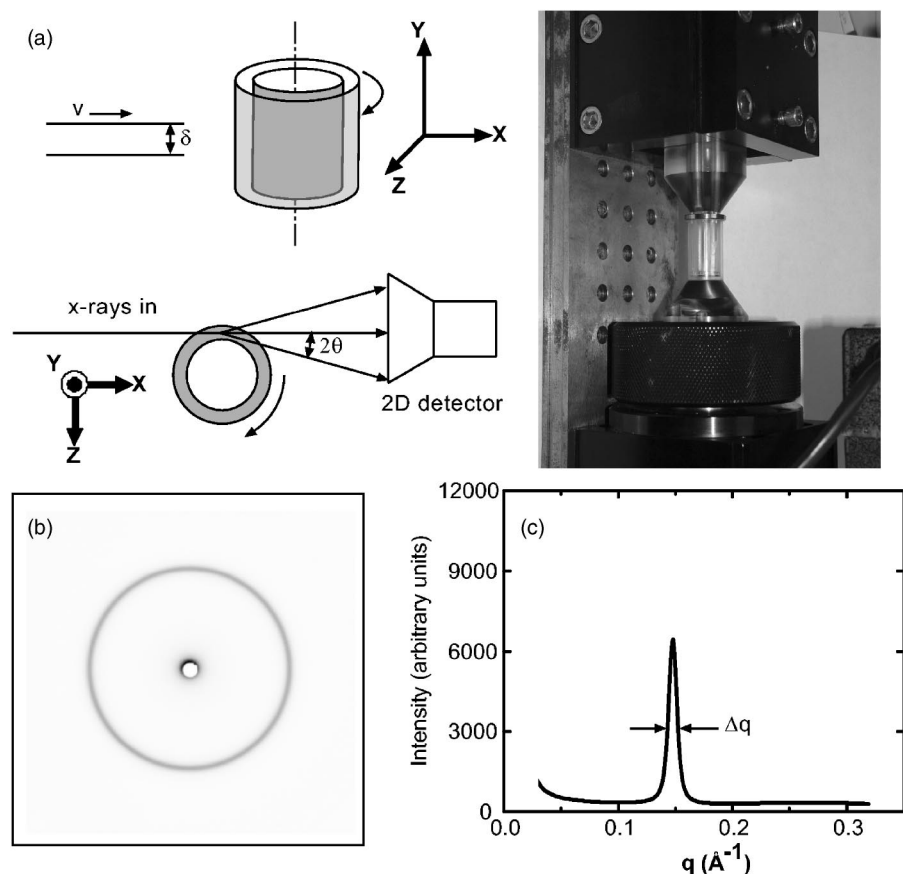
FIG. 2. (a) Photograph and schematic of the experimental setup showing the rotating cylinder geometry, the incident x-ray beam, and the relative location of the two-dimensional x-ray detector. The shear rate $\dot{\gamma} = v/\delta$ is defined by the relative rotational speed of the cylinders. (b) Two-dimensional x-ray diffraction image of the (001) reflection of palm oil in the β' phase. (c) Radially integrated x-ray intensity profile derived from the 2D image showing the peak position q_0 and the peak width Δq.

fraction profiles from the small-angle experiments were then fit to a combination of Gaussian and Lorentzian peak functions using a modified Levenberg-Marquardt algorithm. The IMAGEJ plug-in was also used to obtain azimuthal plots from the 2D diffraction patterns, by plotting the intensity along the circumference (χ angle) of the diffraction rings. This allowed for the evaluation of the crystalline orientation in the crystallizing sample [2].

For an unoriented, polycrystalline material, the area under the x-ray diffraction peak seen in the radial plot, referred to as the integrated intensity, is proportional to the total crystalline mass (also called the solid fat content) of a given phase present in the volume illuminated by the x rays [22]. However, in our measurements taken at higher shear rates, the orientation of the crystallites is observed in the x-ray mosaic scans. As the degree of orientation seen in the diffraction images is not high [full width at half maximum (FWHM) ∼70°] and as there is still considerable unoriented material coexisting with the oriented crystallites, we will make the assumption that the orientation is similarly weak in the direction not probed by our experiments and that this weak orientation does not impact strongly on the relationship between the SFC and total integrated intensity. We therefore will continue under the approximation that the SFC is still proportional to the total integrated intensity, even under conditions of weak orientation.

The determination of an exact proportionality constant between the SFC and integrated x-ray intensity requires their simultaneous determination, or experiments should at least be conducted under similar conditions of heat and mass transfer [23]. For a number of practical reasons this is not technically feasible at the present time for a stationary system and even less for a system under shear. Thus, we estimated an approximate ratio between the SFC and integrated intensity using SFC data for a stationary system at 17 °C provided in the literature as follows.

The SFC of palm oil after being crystallized for 1 h under static conditions in the β' phase was estimated from the data by Ng and Oh [18] to be 25% at 17 °C and 14% at 22 °C, resulting in an average ratio of their measured SFC to our integrated x-ray intensity measurements for phase β' of $S_{\beta'}$ =4.1. The SFC of palm oil at 17 °C crystallized after 7 min (corresponding to the formation of the α phase only) is around 11.5%, corresponding to our integrated intensity of 2.3 normalized units for phase α, yielding a ratio of SFC to integrated intensity S_α=5 for the α crystals.

The position of the diffraction peak, q_0, is related to the thickness of the lamellae (d spacing)—that is, proportional to the longitudinal length $2L$ seen in Fig. 1(a). The full width half maximum of the peak (Δq) is related to the correlation length (D) by the relationship $D=2\pi/(\Delta q)$. For a small single-domain crystallite this correlation length is an approximate measure of the thickness of that crystallite.

III. RESULTS

The images presented in Figs. 3(a) and 3(c), resulting from preliminary wide-angle diffraction experiments, were obtained by subtracting the liquid fat contribution from the total x-ray scattering of wide-angle diffraction patterns at
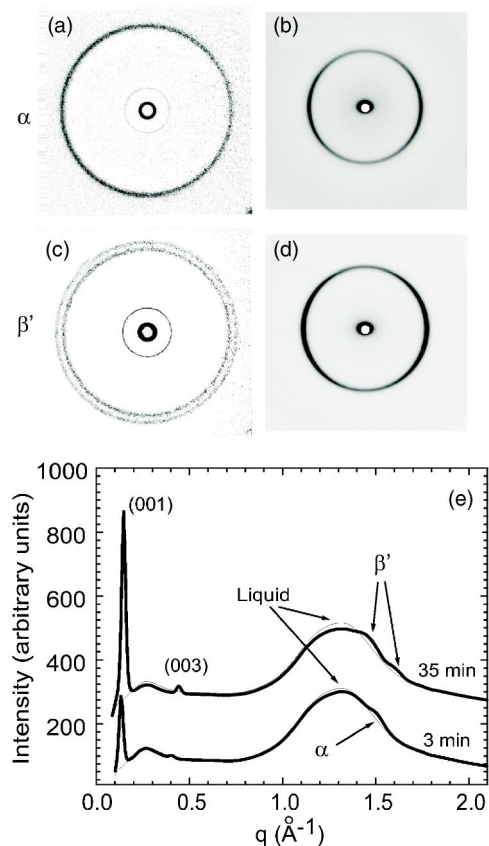
FIG. 3. Two-dimensional diffraction patterns from palm oil crystallized at a final temperature of 17 °C and shear rate of 1440 s^{-1}. Note that the liquid contribution to the scattering has been subtracted to enhance the crystalline diffraction peaks. (a) Wide-angle pattern of phase α (b) Small-angle reflection of phase α showing the peak position at $q=0.134$ Å^{-1}, taken 3 min after the onset of crystallization. (c) Wide-angle pattern of phase β'. (d) Small-angle pattern of phase β' showing the (001) peak position at $q=0.148$ Å^{-1}, taken 35 min after the onset of crystallization. (e) The radially integrated powder diffraction profiles generated from the 2D detector images in (a) and (c) before subtraction of the liquid component can be seen by the thick lines. The thin lines show the diffraction intensity observed from liquid oil, just before the onset of crystallization.

17.5 °C under a shear rate of 1440 s^{-1}. This was done to enhance the image so that the sharp diffraction rings from the crystals could be seen. Normally, these would be difficult to see due to the relatively strong scattering from the large amount of liquid oil present. The characteristic single wide-angle ring of phase α is clearly visible in Fig. 3(a), captured 3 min after reaching 17.5 °C. Similarly, the two rings associated with phase β' are visible in the image captured after 35 min [Fig. 3(c)]. Figure 3(e) shows the radial profiles from the original images (thick lines) compared to the liquid (thin lines). Having characterized the two phases we decided to follow the kinetics of the phase transition using the small-angle (001) reflection that has the higher intensity and suffers less distortion as the diffracted x rays emerge from the cylindrical cell.

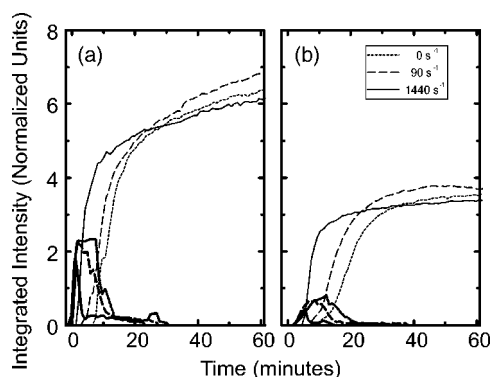Two typical small-angle x-ray diffraction patterns from palm oil crystallized at 17 °C and under a shear rate of

FIG. 4. Plot of the selected integrated intensities of the crystalline phases α (thick lines) and β' (thin lines) taken at different shear rates for final crystallization temperatures of (a) 17 °C and (b) 22 °C as a function of time. The integrated intensity has been normalized to account for sample attenuation and incident x-ray beam intensity variations.

1440 s^{-1} can be seen in Figs. 3(b) and 3(d). A diffraction pattern showing the (001) peak of phase α ($q=0.134$ Å^{-1}), captured 1.3 min after reaching 17 °C, is presented in Fig. 3(b). The diffraction pattern in Fig. 3(d) shows the (001) peak of phase β' ($q=0.148$ Å^{-1}), captured 31.9 min after reaching 17 °C. Both patterns display a clear weak preferred orientation of the crystals in the (001) peak. The diffuse x-ray scattering from the crystallites seen around the beam-stop is elliptic in both patterns, consistent with the preferred orientation of the particles. The diffraction patterns captured without shear, in contrast, appeared as isotropic rings, with no preferred orientation. The radially averaged plots of the (001) diffraction peak obtained from the diffraction patterns allowed us to differentiate and quantify both phases.

A. Onset times

The integrated x-ray diffraction peak intensities were used to follow the kinetics of the various phase transitions, two from the liquid to the crystal and one between the crystalline phases. Typical data demonstrating these phase transitions is shown in Figs. 4(a) and 4(b), where the growth of the α phase (heavy line) and β' phase (light lines, longer times) is represented by plotting x-ray integrated intensity as a function of time. Figure 4(a) shows the crystal growth behavior of palm oil crystallized at 17 °C at three shear rates—namely, 0, 90, and 1440 s^{-1}—while Fig. 4(b) shows the behavior at 22 °C. The origin of the time scale of the graphs is the moment when the shear cell reached the crystallization temperature of 17 or 22 °C.

The average onset time of crystallization (the time from the moment that the system reaches the target crystallization temperature to the first evidence of crystallization) into phase α was negative ($t_{o\alpha}=-0.3\pm0.1$ min—i.e., 18 °C); that is, the material started crystallizing before the cell reached 17 °C. Similarly, the onset time of crystallization at 22 °C was very short ($t_{o\alpha}=1.7\pm0.2$ min). There was no obvious effect of the applied shear on the onset time of crystallization of phase α. Phase β' appeared some time after the onset of phase α, and
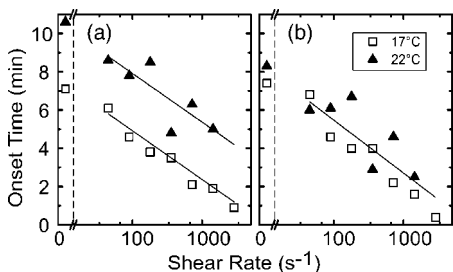
FIG. 5. Plot of the onset times of the formation of the β' phase as a function of applied shear rate measured from the time of reaching the final crystallization temperature (a) and measured from the onset of the formation of phase α (b), showing the universal behavior in (b).

the intensity of phase α started to decrease simultaneously to the increase in the proportion of phase β'.

As the applied shear increased, the time it took for the phase α to transform to phase β' was reduced at both temperatures. There was an obvious acceleration of the phase transition from phase α to phase β'; however, there was no obvious change in the onset time of nucleation for phase α. In most cases we observed that a small amount of phase α survived for some time after the transition from phase α to phase β', as evidenced by a slight asymmetry in the β' (001) diffraction peak. We will ignore this small residual amount of α phase in our future discussions. The maximum intensity reached by phase α did not depend much on the shear rates and was about 2.3 in our normalized x-ray intensity units (2.3 nu) at 17 °C, except for the experiments at 1440 s^{-1} and 2880 s^{-1}, where the x-ray intensities were 1.8 and 1.1 nu, respectively. At 22 °C the maximum observed intensity was around 0.6 nu for all shear rates.

The onset times for the appearance of the β' phase ($t_{o\beta'}$) in Fig. 5 were estimated from the fitting procedure of the crystallization process described later in the next section but are roughly the same when the first β' diffraction peaks were observed. The triangles represent β' onset times at 22 °C and the squares at 17 °C. The times under static conditions (0 s^{-1}) have been plotted at the left edge of the graph, for comparison. The data for the onset times with respect to the moment the system reached the crystallization temperature are plotted in Fig. 5(a) as a function of the logarithm of the shear rate. The data points of the sheared experiments can be fit to straight lines, as shown in the figure. As we have previously reported [2], the reduction in the onset time of the phase transition induced by shear seems to be a universal effect in all phase transitions of fats, for reasons that will be discussed later in this paper. Observing that the lines are roughly parallel, we plotted the onset times for phase β' with respect to the onset time of phase α, and the data collapsed into a single line [Fig. 5(b)]. It thus appears that the onset time of nucleation for phase α is affected by the crystallization temperature, but not by shear, while the relative onset time for phase β' does depend on the shear rate.

The effect of shear ($\dot{\gamma}$) and temperature (T) on the onset times t_o can be summarized by two simple equations

$$t_{o\beta'} = -m \ln(k_t \dot{\gamma}), \tag{1}$$

$$\frac{\Delta t_{o\alpha}}{\Delta T} \approx \left. \frac{\partial t_{o\alpha}}{\partial T} \right|_{(17<T<22)\,°C} = b, \tag{2}$$

where m is 1.2 min, k_t is 1.05×10^{-4} s, only valid for shear rates above 15 s^{-1} where it intercepts the $t_{o\beta'}$ value for zero shear, and b is 0.4 min/°C.

B. Integrated intensity and crystalline fraction

We will now propose a comprehensive approach to the modeling of the phase transitions involving the liquid and both phases α and β', using a modified differential form of the Avrami growth function.

At each temperature and composition of the liquid there is a certain driving force to crystallize to a particular composition of β', and if the temperature is below 24 °C, also to crystallize to a given composition of α.

The driving force is a function of the supersaturation or undercooling, ideally the difference in chemical potential between the liquid with the current composition and the solid in equilibrium with that liquid. However, since we do not have compositional data during crystallization, we will use a "brute force" approach and define the driving force σ as the ratio between the mass of the uncrystallized material (liquid) and the total mass of the material potentially crystallizable. The SFC, C_{SF}, values were estimated by multiplying the integrated intensities by the ratios S_α and $S_{\beta'}$ mentioned above. We will denote the equilibrium value that the C_{SF} tends to by C_{SF}^*.

$$\sigma \approx \frac{C_{SF}^* - C_{SF}}{C_{SF}^*} = 1 - \frac{C_{SF}}{C_{SF}^*}. \tag{3}$$

If the time is measured from the onset of the process that is being modeled, the untransformed material fraction (e.g., liquid) $L = C_{SF}^* - C_{SF}$ follows the differential form of the Avrami equation given by

$$\frac{\partial L}{\partial t} = -nkL \left[-\ln \left(\frac{L}{C_{SF}^*} \right) \right]^{(n-1)/n}, \tag{4}$$

where k is a time scaling constant and n is a growth mode exponent. Thus, the rate at which the phase transition occurs is a function of the amount of material left in the phase being transformed, be it the liquid or the metastable phase α.

To visualize this, the total mass of liquid fat is represented in Fig. 6 by the area of a rectangle that is divided into several columns, the width of each column proportional to the amount of a given fraction or molecular species. The leftmost columns represent high melting fractions, while the rightmost represent low melting fractions. The height of the column can be distributed among the liquid and one or more crystalline phases.

At the initial stages of crystallization, the material that crystallizes from the melt produces α crystallites consuming part of the high melting fraction available for crystallization in the α phase. Taking the typical composition of industrial palm oil stearin as a reference [9], the solid fraction is represented by the white area in Fig. 6. This area, which we denote by mass fraction A^*, is ca. 12% of the total area in
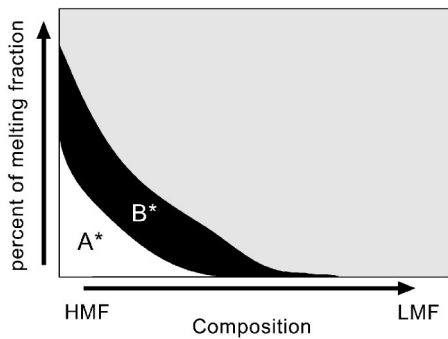
FIG. 6. Schematic of the compositional fractions in the liquid phase of palm oil. See the text for details.
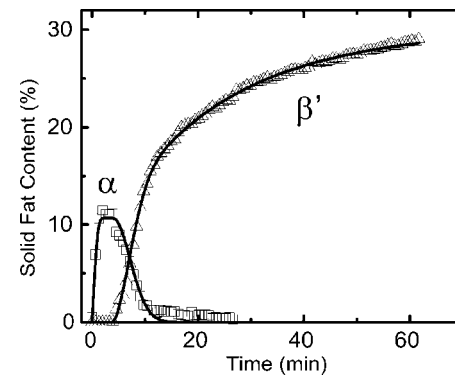

FIG. 7. Plot of the solid fat content (SFC) of phases α (squares) and β' (triangles) of palm oil crystallized to a final temperature of 17 °C and under a shear rate of 90 s^{-1} as a function of time. The solid line represents the model fit to the crystal growth given by Eqs. (5)–(7).

this example. Additional liquid can be crystallized into the β' phase, as shown in Fig. 6 by the black region. This black region is denoted by mass fraction B^*. The two regions therefore represent the maximum crystallizable liquid that can go, at a given temperature, into each one of the phases. The total amount of crystallizable liquid that can go into the β' phase is A^*+B^*. The area of A^*+B^* in the sketch is ca. 29% of the total area.

We postulate that the phase behavior of the crystallizing fats goes as follows: Phase α nucleates from the melt and grows from fraction A^*. At some later time, which depends on the shear rate, the α crystals act as nucleation sites for the formation of β' crystals, which grow at the expense of α crystallites as well as from the melt fractions A and B.

Due to the growth of phase α, the material available from region A^* in Fig. 6 will become depleted, leaving behind the uncrystallized portion A; i.e., the amount of crystallized α phase is $\alpha_{SFC}=A^*-A$. If the time is long enough, all A^* becomes crystalline, as observed in the plateau reached by phase α in the static experiment at 17 °C and 0 s^{-1} seen in Fig. 4(a). If by the time that β' starts to grow there is liquid available from both regions A^* and B^* in Fig. 6, the β' phase will crystallize out of both fractions, assuming the liquid is homogeneous. This will reduce both amounts of fractions A and B, the uncrystallized portions of both regions. We will assume that the amount of phase β' that crystallizes from each one of the regions is proportional to the amount of liquid material of that region still present at a given time; i.e., the fraction of β' coming from A is $A/(A+B)$ and the fraction coming from B is $B/(A+B)$.

Thus the process can be modeled with three simultaneous differential equations (5)–(7), shifting the data to a time origin coincident with the onset of phase α. In these sets of equations, n_a and k_a refer to the Avrami constants describing the transformation of A to α and n_b and k_b refer to the constants describing the rate that β' is formed from the melt $(A+B)$, while n_c and k_c refer to the rate at which α transforms into phase β'.

Equation (5) describes the consumption of the liquid fraction A, as it is converted into phase α, and into phase β' after the onset time of β' formation, $t_{o\beta'}$.

Equation (6) describes the formation of phase a from the liquid fraction A and its disappearance as it transforms into phase β' after $t_{o\beta'}$. The solid phase transition in crystals can in some cases of constant temperature be modeled with the same Avrami function used to describe liquid-solid transformations [24]:

$$\frac{\partial A}{\partial t} = -n_a k_a A \left[-\ln\left(\frac{A}{A^*}\right) \right]^{(n_a-1)/n_a} - \left\{ n_b k_b (A+B) \right.$$
$$\left. \times \left[-\ln\left(\frac{A+B}{A^*+B^*}\right) \right]^{(n_a-1)/n_a} \frac{A}{A+B} \right\}_{t>t_{o\beta'}}. \quad (5)$$

Equation (6) describes the formation of phase a from the liquid fraction A and its disappearance as it transforms into phase β' after $t_{o\beta'}$. The solid phase transition in crystals can in some cases of constant temperature be modeled with the same Avrami function used to describe liquid-solid transformations [24]:

$$\frac{\partial \alpha_{SFC}}{\partial t} = n_a k_a A \left[-\ln\left(\frac{A}{A^*}\right) \right]^{(n_a-1)/n_a} - \left\{ n_c k_c \alpha_{SFC} \right.$$
$$\left. \times \left[-\ln\left(\frac{\alpha_{SFC}}{A^*}\right) \right]^{(n_c-1)/n_c} \right\}_{t>t_{o\beta'}}. \quad (6)$$

Equation (7) describes the crystallization of the liquid fraction B into phase β':

$$\frac{\partial B}{\partial t} = -\left\{ n_b k_b (A+B) \left[-\ln\left(\frac{A+B}{A^*+B^*}\right) \right]^{(n_a-1)/n_a} \frac{B}{A+B} \right\}_{t>t_{o\beta'}}. \quad (7)$$

The amount of β' can be computed at any time by the mass balance equation

$$\beta'_{SFC} = (A^*+B^*) - (A+B) - \alpha_{SFC}. \quad (8)$$

The initial conditions are $A(t=0)=A^*$, $B(t=0)=B^*$, and $\alpha_{SFC}(t=0)=0$. The system of simultaneous differential equations was integrated numerically using a routine for stiff differential equations provided by MATLAB. The MATLAB simplex algorithm was used to optimize the nine parameters $t_{o\beta'}$, $k_{(a,b,c)}$, $n_{(a,b,c)}$, A^*, and B^* by minimization of the χ^2 function between the SFC derived from the experimental data for each phase and the SFC computed from the model given by either α_{SFC} or β'_{SFC}. The fits were remarkably good for the experiments at 17 °C as seen in Fig. 7 and somewhat less

TABLE II. Parameters $t_{o\beta'}$ and C^*_{SF} from the fitting procedure.

T (°C)	$\dot{\gamma}$ (s^{-1})	$t_{o\beta'}$ (min)	A^* (%SFC)	(A^*+B^*) (%SFC)
17	0	7.4	12	30
	45	6.8	11	30
	90	4.6	10	29
	180	4.0	9.7	29
	360	4.0	10	27
	720	2.2	10	29
	1440	1.6	8.3	30
	2880	0.35	7.8[a]	16[a]
Average			10.1±0.4	29±1.7
22	0	8.3	3.7	15
	45	6.0	3.6	16
	90	6.1	3.9	15
	180	6.7	3.7	14
	360	2.9	4.5	15
	720	4.6	5.9	14
	1440	2.5	6.2	14
Average			3.9±0.4	15±0.3

[a]Excluded from the average.

accurate for the experiments at 22 °C. The resulting values for the optimized parameters are reported in Tables II and III.

The average values of the quantity (A^*+B^*), which represents the final total SFC of the β' phase at 17 and 22 °C (29% and 15%, respectively) are consistent with data in the literature [18]. The extrapolation of A^* to zero yields a melt-ing temperature of 25 °C for phase α, while for (A^*+B^*) the extrapolation to zero gives a value of 27 °C for phase β', which are close to the values in the literature (of 24 and of 26–28 °C, respectively) [7]. The data at 2880 s^{-1} produced a value of (A^*+B^*) different from the other 17 °C values and similar to the 22 °C values, which can only be explained by

TABLE III. Parameters k and n from the fitting procedure.

T (°C)	$\dot{\gamma}$ (s^{-1})	k_a	n_a	k_b	n_b	k_c	n_c
17	0	1.0	1.6	0.051	0.69	0.27	1.2
	45	0.70	2.1	0.059	0.75	0.26	1.3
	90	1.6	1.4	0.056	0.80	0.20	1.7
	180	1.7	1.8	0.068	0.68	0.21	2.5
	360	0.78	2.4	0.093	0.76	0.36	1.4
	720	1.8	1.7	0.12	0.55	0.43	1.7
	1440	2.2	1.8	0.10	0.33	0.76	1.0
	2880	1.8	1.8	0.12	0.92	0.50	1.8
Average		1.4	1.8	0.083	0.69	0.37	1.6
Std. Err.		0.2	0.1	0.010	0.06	0.07	0.2
22	0	0.29	1.7	0.027	3.2	0.11	2.8
	45	0.29	1.7	0.024	3.1	0.11	2.9
	90	0.27	1.5	0.029	3.6	0.10	2.9
	180	0.23	1.2	0.038	4.4	0.12	3.2
	360	0.49	1.1	0.028	4.5	0.13	3.7
	720	0.22	1.4	0.037	5.3	0.11	6.9
	1440	0.35	1.2	0.033	3.5	0.09	5.8
Average		0.31	1.4	0.031	3.9	0.11	4.0
Std. Err.		0.03	0.1	0.002	0.3	0.00	0.6

an effective increase in temperature due to viscous heating.

The values of the time constants and the growth exponents are summarized in Table III. Most values did not show a particular trend dependent on the shear rate applied, but were dependent on temperature. The values of k_b at 17 °C, however, showed an increasing tendency with shear indicating that the growth of the β' crystals was influenced by shear. At 22 °C the time constants k were all lower, consistent with less undercooling producing a smaller driving force.

The values of the growth exponents n are indicative of the type of growth that is occurring in the crystalline system [25]. The values of n_a are certainly more reliable at the lower shear rates, where more intensity and data points were available for the growth of the metastable phase α; thus, it is not clear that there is a significant difference between n_a at both temperatures. Both n_b and n_c increased significantly with the increase in temperature, indicating that different growth regimes were taking place at the two temperatures, as discussed in further detail later.

C. Diffraction peak position and phase composition

The peak position for phase α at 17 °C ranged from $q = 0.1340$ Å^{-1} at the onset of crystallization to $q = 0.1346$ Å^{-1}. At 22 °C this range was from 0.1345 Å^{-1} at the onset to 0.1356 Å^{-1}. This peak position corresponds to a lamellar thickness of 46.7 Å at 17 °C and 46.3 Å at 22 °C, both of them consistent with a $2L$ longitudinal packing. The correlation between peak position and composition has been illustrated for binary and ternary mixtures of POP, POS, and SOS [26–28] and was discussed by us in a recent report on the crystallization of milk fat [29]. Essentially, the size of the molecules depends on the lengths of the fatty acids that constitute the TAG. For a fraction constituted by molecules with more or less similar melting points, the larger molecules will be preferentially incorporated into the crystal. However, this will deplete the interface precisely of those molecules, and thus, over time the proportion of smaller molecules increases, as reflected by the increase of peak position, corresponding to a decrease in lamellar thickness. The competition between the rate of incorporation into the crystal and diffusion from the bulk into the interface, often called "the two-step crystallization process" [30], will thus determine the actual compositional path of the crystallization process. Under static conditions, the crystalline growth is mostly controlled by the transport of molecules to the interface; i.e., it happens at the diffusion limit. In the presence of shear, the incorporation rate becomes more important as the shear rate increases, until it becomes the controlling mechanism.

The β' phase presented an even larger variation in peak position over time, particularly during the initial growth period, corresponding to a change in d spacing from 44.9 Å at the onset to 42.4 Å—i.e., 2.5 Å at 17 °C. This corresponds to a very large variation in the average composition of the crystals. On average, the peak positions at 22 °C were higher than at 17 °C for the same shear rate, as seen in Fig. 8. Therefore, the molecular species in the crystallites at 22 °C formed smaller or better packed crystalline layers, indicating
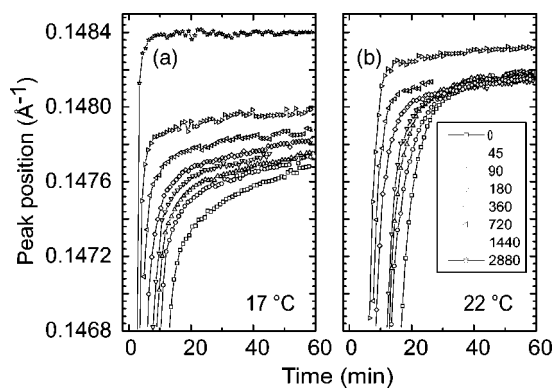

FIG. 8. Plot of the (001) x-ray diffraction peak positions of the β' phase for different shear rates as a function of time after reaching the final crystallization temperature of (a) 17 °C and (b) 22 °C.

that the lamellar thickness was decreasing, probably due to the smaller size of the molecules preferentially crystallizing from the melt.

At 17 °C the peaks are well discriminated by the shear even 40 min after reaching the crystallization temperature. The peak positions come progressively closer at longer times, since almost all the crystallizable material has been incorporated into the solid phase. At 22 °C the peaks are discriminated by shear only during the first 20 min, after which only the 1440 s^{-1} peak position remains apart. Since the peak position is an averaged consequence of the composition of the whole crystalline mass sampled by the x rays, this is consistent with the average composition trajectory that is different only at the beginning of the process at 22 °C, becoming uniform as most of the crystallizable material has become solid. Of course the difference in the final average layer spacing measured at 17 and 22 °C is expected, as the fractions A^* and B^* will change with temperature.

Even if at a given temperature the final average peak position (or average composition) was the same for all shear rates, the different paths would likely produce a different structure in the crystallites, in a similar fashion that fats crystallized under different conditions produce very different microstructures even if they have the same final SFC [31,32]. The crystallites formed under high shear rates would likely show a smaller gradient in composition and d spacing (from core to surface) than the material crystallized at lower shear rates due to better mixing of the melt and a reduced boundary layer surrounding the crystallites. When considering fractionation applications the lower shear rates would seem attractive, even if the times to reach the maximum were longer. On the other hand, if stability is desired, perhaps higher shear rates would be more useful.

The curve for 2880 s^{-1}, nominally at 17 °C, was probably at a higher effective temperature due to viscous heating, as seen by its decreased SFC, compared to other shear rates at 17 °C. A different final composition was therefore likely achieved. The growth of the integrated intensity curve at 2880 s^{-1} was very small but positive similar to the curve seen for 22 °C in Fig. 4(b). Since the correlation length of the (001) diffraction peak was still increasing, it would seem that the crystallites were growing with no compositional

change, having reached a regime where the composition of the liquid being crystallized was the same as the solid.

It can be seen that at 22 °C the peak position q had a higher value than at 17 °C, and its value was also slightly higher at the higher shear rates. This variation points to different conditions of molecular segregation during the crystallization: at higher temperature or higher shear rate the molecules crystallized resulted in smaller lamellar thicknesses, very likely because they are smaller molecules. This molecular segregation, also referred to as fractionation, is probably the consequence of the different mass transfer conditions between the liquid and the crystallizing solid.

Fractionation occurs at the crystallization interface because of the difference in concentration of the melting fractions between the bulk liquid and the layer of crystalline material, caused by their different free energies of crystallization. Since the high melting fraction tends to crystallize more readily that the other fractions, the concentration it attains on the surface of the crystal $[HMF]_{ci}$ is higher than the concentration in the melt in contact with the crystal $[HMF]_{li}$. The opposite happens with the other fractions. Thus the conditions at the interface can be stated as

$$[HMF]_{li} < [HMF]_{ci}$$

$$[LMF + MMF]_{li} > [LMF + MMF]_{ci}, \qquad (9)$$

where $[LMF]$ and $[MMF]$ represent the concentrations of the low and medium melting fractions, respectively. The preferential crystallization of the HMF depletes the interface of the HMF; thus, its concentration would be lower than that of the HMF in the bulk. The difference in composition between the bulk melt and the liquid at the interface, therefore, will be the opposite:

$$[HMF]_{bulk} > [HMF]_{li}$$

$$[LMF + MMF]_{bulk} < [LMF + MMF]_{li}. \qquad (10)$$

Under these conditions, the HMF tends to diffuse from the bulk to the interface, while the other species tend to go away from the interface. The effect of increasing shear is a reduction of the concentration difference between the bulk and the interface, resulting in a higher proportion of HMF material being crystallized at any given time. In the particular case of palm oil, the average molecular size of the HMF material is smaller than the other two melting fractions. An increase in shear results in an increase of the HMF proportion near the interface, therefore resulting in a smaller d spacing. However, as more material is crystallized, the averaged resulting lamellar sizes may all become similar between the resulting crystalline materials, even if the distribution of TAG's between crystals is different due to the different paths followed.

D. FWHM, correlation length, and crystalline thickness

The reduction in the FWHM (Δq) of the (001) diffraction peaks as time progresses is indicative of growth of the crystals in the c direction—i.e., growth in their thickness—as
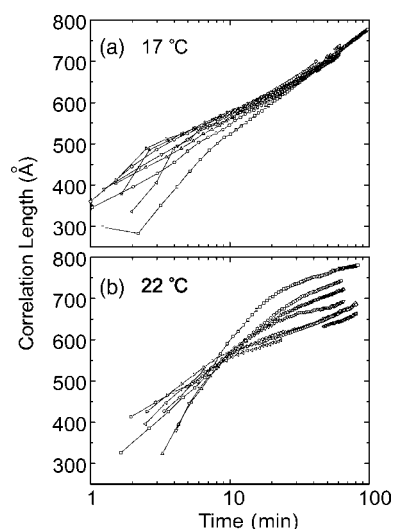

FIG. 9. Plot of the correlation length derived from the (001) reflection of the β' phase as a function of time for different shear rates and final crystallization temperatures of (a) 17 °C and (b) 22 °C. The symbols correspond to the same shear rates described in Fig. 8.

shown in plots of correlation length $D = 2\pi/\Delta q$ in Fig. 9 for phase β'. However, it is not necessarily a straightforward relationship. The narrowing of Δq is a direct consequence of the increase in the correlation length of the domains inside the crystal, rather than of the actual thickness, unless the crystal is a single domain [22], in which case it is the thickness of the crystal.

The α phase crystallites had a correlation length of 100 Å at 17 °C and 91 Å at 22 °C, which corresponds to only two lamellar thicknesses. This suggests that they are not only thin crystals, but also that their degree of order is low, consistent with their being in a metastable phase.

In most experiments the ratio between correlation length and lamellar thickness (i.e., d spacing) for phase β' started at values of D/d between 5 and 8. It then grew to values between 15 and 17 lamellae per domain.

It would seem that as the crystals grow, the newly incorporated lamellae have much less variation in d spacing, as can be observed from the peak position variation. The variation in peak position slowed down earlier and at higher values as the shear rate was increased, as was explained in the previous section. At 17 °C all peak widths have reached approximately the same value after 60 min, still larger than the instrumental resolution.

It may be suspected that the orientation of the crystallites is responsible for the observed effect of shear on correlation length. However, the variation of correlation length with shear was also observed in the low-shear-rate experiments, where no preferred orientation of the crystallites was detectable.

When the correlation length was plotted against the logarithm of time [Figs. 9(a) and 9(b)], a common behavior was observed for the experiments at 17 °C and for the experiments at high shear rates at 22 °C. The growth of the correlation length became linear with $\log(t)$ above a certain value. At 17 °C this log-linear behavior started early on, at corre-
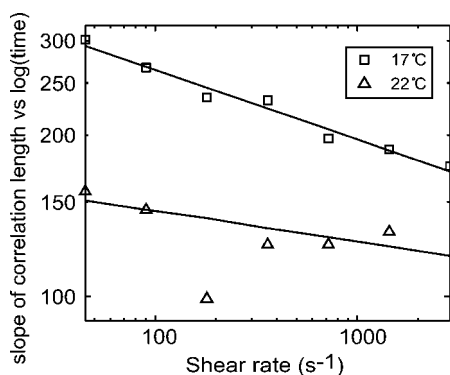
FIG. 10. Plot of the slope of the correlation length versus logarithm of time plots seen in Fig. 9 as a function of shear rate for final crystallization temperatures of (a) 17 °C and (b) 22 °C. The point for 22 °C at 180 s^{-1} was not included in the fit.
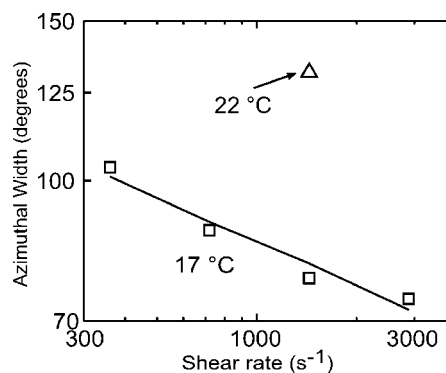

FIG. 11. Plot of the azimuthal width $\Delta\chi$ derived from the mosaic scans of all samples of palm oil that could be oriented, showing the orientation improving with shear rate.

lation length values between 480 Å and 550 Å, increasing slightly as the shear decreased. At 22 °C it started around 550 Å for the higher shear rates and increased until 750 Å. When palm oil is fractionated at slow cooling rates, a break in the yield curve occurs at 18 °C, attributed to the change of regime induced by the inclusion of the lower melting fractions in the crystallizing mass [15]. Therefore, since our experiments were carried out at a higher cooling rates, it is reasonable that this inclusion becomes more important, and thus there are differences in the mechanisms at both temperatures.

The slopes of the log-linear regions as a function of shear rate are plotted in Fig. 10. The dependence of the correlation length D on shear rate and time can be described by

$$\frac{\partial D}{\partial t} = \frac{a\gamma^{-b}}{t}, \quad (11)$$

where $a=480$ and $b=0.13$ at 17 °C and $a=190$ and $b=0.06$ at 22 °C. As discussed before, the growth in crystallite thickness may follow a behavior similar to the one described for the correlation lengths. Recall that the crystallites that form from the melt in a fat are typically plate like, with the long axis of the TAG molecule perpendicular to the flat side of the plate. If the platelike structure is treated as an ideal cylinder, the aspect ratio of the crystal can be defined by A/D, where A is the area of one of the end caps of the cylinder, while D is the length (or thickness) of the cylinder. The value of the ratio between the integrated intensity (proportional to the total crystalline volume, $V=AD$) and the correlation length (which we assume is related to the thickness of the crystallites, D) is roughly proportional to the total surface area of one flat side of the crystallites. It turns out that this "effective area" plateaus approximately at the same point where the curves of correlation lengths become log-linear. Since the thickness and the total integrated intensity are still growing, this plateau of the effective area can be interpreted as the absence of lateral growth of the crystallites, meaning that the growth observed in this stage happens mostly in the direction perpendicular to the lamellae; in other words, the plate like crystals get thicker. This should be consistent with a situation when no nucleation is present and the

growth index is equal to 1, although care is to be exercised in the interpretation of these values since they are obtained from a single curve and in conditions quite different from those of the original Avrami model [25]. The values of n_b obtained at 17 °C are not too far from unity. The values of n_b at 22 °C, where the fits are less accurate have to accommodate the change in the regime of growth dimensionality, and that explains that their values are considerably larger.

E. Crystalline orientation under shear

As we reported before [2], shear can induce orientation in crystallizing fats. In the case of palm oil clear orientation was only observed at 17 °C and shear rates of 360 s^{-1} or greater and at 22 °C only at a shear rate of 1440 s^{-1}. This orientation is also a manifestation of the fact that the agglomeration forces between crystallites have been overcome by the shearing forces, allowing the crystallites to segregate.

The azimuthal profiles of the oriented samples showed two peaks separated by 180°, which were fit to Gaussian functions. The value of the FWHM of these orientational plots, $\Delta\chi$, was almost constant over time during the course of each one of the experiments at 17 °C at a particular shear rate, but varied with shear rates as seen in Fig. 11. The value of the break point in the orientation behavior at 360 s^{-1} suggests a threshold for the competition between agglomeration and segregation of the crystallites. At the end of a few experiments at a low shear rate, the shear rate was increased suddenly for a short time before melting the paste and an immediate increase in orientation was observed, suggesting that even in those cases the crystallites were only loosely aggregated.

As explained in [2], the necessary shear rate to orient free crystallites at the onset of the phase α crystallization is related to the competition between the shear forces and the rotary diffusivity of the crystalline nuclei, described by their ratio in the Peclet number.

At higher volume fractions and larger (non-Brownian) crystallite sizes, the interactions between crystallites (attraction and collisions) are the cause of the randomization in the directionality of the crystallites. Thus, the uniformity of the diffraction patterns results from the prevalence of those randomizing mechanisms over the shear applied. As a certain

level of shear is reached, shear forces are sufficiently large to start inducing the orientation, probably on the portion of the crystallite population with larger aspect ratios and sizes. This orientation is thus related to a segregation of a certain proportion of crystallites from the spherical clusters, that would otherwise tumble in the fluid.

IV. DISCUSSION

There is no clear mechanism in the literature thus far to fully account for the phase transition acceleration, although it has been suggested that shear could be orienting the molecules to favor a particular polymorph [33,34]. This is not really feasible, because the shear rates used are far too small to be causing any direct molecular orientation in these materials. The liquid drag forces on the surfaces of the crystallites are also too small to cause enough strain on the crystallite surface to induce the phase transition acceleration. Changes in local and overall composition caused by the effect of shear on the diffusive mechanisms near the crystallites, as described earlier, may account for a small acceleration. Different shear rates produce crystallites that follow different compositional trajectories as they grow, at least in the β' phase. However, the position and width of the diffraction peak for the metastable phase α did not show significant differences at the different shear rates studied. It seems therefore unlikely that the acceleration mechanism depends only on the different composition of the liquid phase, even though the crystallization proceeds via somewhat different compositional paths at the different shear rates.

Since no obvious acceleration effect from shear was observed in the nucleation of α from the melt, it seems that under our experimental conditions shear did not affect the liquid structure as far as nucleation is concerned; i.e., shear was not acting directly at a molecular level. Therefore, the acceleration of the onset of phase β' is neither likely due to such direct action of shear on the liquid structure. Also, as shear did not affect the onset time of the α phase crystallizing from the melt, the fact that the onset time of β' does strongly depend on shear rate suggests that the β' phase does not just undergo homogeneous nucleation from the melt.

A possible explanation of the phase transition acceleration arises from the aggregation-segregation competing mechanisms discussed earlier. Under static conditions and at lower shear rates, the α crystallites form clusters that provide less nucleation sites per unit volume for the onset of the phase β'. At higher shear rates, the crystallites are segregated and provide a much larger surface area in contact with the liquid, and they also come in contact with different regions of liquid at a higher frequency, thus increasing the possibility of acting as nucleation sites for the formation of β'. Thus, the heterogeneous nucleation of phase β' from the melt takes place on the already existing α crystallites. This also means that the heat of crystallization released by the forming β' crystallites is received primarily by the α crystallites, and thus the α to β' transformation happens readily.

To conclude, we have discussed the crystallization behavior of palm oil from the melt under dynamic conditions of shear. The phase transition from the metastable α phase to the more stable β' phase was accelerated by shear. This effect can be explained by a simple model where the α crystallites nucleate and grow from the melt, a process which occurs independently of shear rate. The α phase grows according to an Avrami growth model. The β' phase nucleates on the α crystallites, with the amount of β' crystal formation dependent on the rate of transformation of α to β' as well as the rate that the β' phase grows from the melt. The shear induced α-β' phase transition acceleration occurs because under shear, the α nuclei form many distinct small crystallites which can easily transform into β', while at lower shear rates, the α nuclei can aggregate together, retarding the nucleation of the β' crystals.

This represents the first time that a quantitative model has been applied to the problem of shear induced phase acceleration in fats. This model should be widely useful to predict the final properties of crystallization of palm oil, based on shear rates, and processing temperatures.

[1] G. Mazzanti, S. E. Guthrie, E. B. Sirota, A. Marangoni, and S. H. J. Idziak, Cryst. Growth Des. **4**, 409 (2004).

[2] G. Mazzanti, S. E. Guthrie, E. B. Sirota, A. G. Marangoni, and S. H. J. Idziak, Cryst. Growth Des. **3**, 721 (2003).

[3] G. Mazzanti, S. E. Guthrie, E. B. Sirota, A. G. Marangoni, and S. H. J. Idziak, in *Soft Materials—Structure and Dynamics*, edited by J. R. Dutcher and A. G. Marangoni (Dekker, New York, 2004).

[4] K. Sato, Chem. Eng. Sci. **56**, 2255 (2001).

[5] S. D. MacMillan *et al.*, Cryst. Growth Des. **2**, 221 (2002).

[6] W. L. Siew and W. L. Ng, J. Oil Palm Res. **12**, 1 (2000).

[7] C. P. Tan and Y. B. Che Man, Food Chem. Toxicol. **76**, 89 (2002).

[8] W. K. Busfield and P. N. Proschogo, J. Am. Oil Chem. Soc. **67**, 171 (1990).

[9] Y. B. Che Man, T. Haryati, H. M. Ghazali, and B. A. Asbi, J. Am. Oil Chem. Soc. **76**, 237 (1999).

[10] E. B. Sirota and A. B. Herhold, Science **283**, 529 (1999).

[11] K. Sato, S. Ueno, and J. Yano, Prog. Lipid Res. **38**, 91 (1999).

[12] K. Kawamura, J. Am. Oil Chem. Soc. **56**, 753 (1979).

[13] K. Kawamura, J. Am. Oil Chem. Soc. **57**, 48 (1980).

[14] K. Kawamura, J. Agric. Chemi. Soci. J. **57**, 475 (1983).

[15] W. L. Siew and W. L. Ng, J. Am. Oil Chem. Soc. **72**, 591 (1995).

[16] B. Jacobsberg and O. C. Ho, J. Am. Oil Chem. Soc. **53**, 609 (1976).

[17] F. V. K. Young, in *Palm Oil*, edited by F. D. Gunstone (Wiley, New York, 1987).

[18] W. L. Ng and C. H. Oh, J. Am. Oil Chem. Soc. **71**, 1135 (1994).

[19] O. Zaliha, C. L. Chong, C. S. Cheow, A. R. Norizzah, and M. J. Kellens, Food Chem. Toxicol. **86**, 245 (2004).

[20] K. P. A. M. Vanputte and B. H. Bakker, J. Am. Oil Chem. Soc. **64**, 1138 (1987).

[21] W. S. Rasband, computer code IMAGEJ, National Institutes of Health, Bethesda, MD, USA, 1997–2004.

[22] B. D. Cullity and S. R. Stock, *Elements of X-ray Diffraction*, 3rd ed. (Prentice-Hall, Englewood Cliffs, NJ, 2001).

[23] A. G. Marangoni, A. J. Wright, S. S. Narine, and R. W. Lencki, J. Am. Oil Chem. Soc. **77**, 565 (2000).

[24] L. Kerschhofer *et al.*, Miner. Mag. **62**, 617 (1998).

[25] A. G. Marangoni, J. Am. Oil Chem. Soc. **75**, 1465 (1998).

[26] T. Koyano, Y. Kato, I. Hachiya, and R. Umemura, J. J. Oil Chem. Soci. **42**, 453 (1993).

[27] A. Minato, S. Ueno, K. Smith, Y. Amemiya, and K. Sato, J. Phys. Chem. B **101**, 3498 (1997).

[28] K. Sato *et al.*, J. Am. Oil Chem. Soc. **66**, 664 (1989).

[29] G. Mazzanti, S. E. Guthrie, E. B. Sirota, A. G. Marangoni, and S. H. J. Idziak, Cryst. Growth Des. **4**, 1303 (2004).

[30] J. W. Mullin, *Crystallization*, 3rd ed. (Butterworth-Heinemann, Oxford, 1993).

[31] S. S. Narine and A. G. Marangoni, Phys. Rev. E **59**, 1908 (1999).

[32] S. S. Narine and A. G. Marangoni, Phys. Rev. E **60**, 6991 (1999).

[33] G. Ziegleder, Int. Z. Lebensm. Tech. Verfahrenst. **36**, 412 (1985).

[34] E. Windhab, E. Niediek, and L. Rolfes, Susswaren. **3**, 32 (1993).